Supplementary Material for

Long-term drying of Mars by sequestration of ocean-scale volumes of water in the crust

E. L. Scheller*, B. L. Ehlmann, R. Hu, D. J. Adams, Y. L. Yung

*Corresponding author. Email: eschelle@caltech.edu

Published 16 March 2021 as *Science* First Release
DOI: 10.1126/science.abc7717

This PDF file includes:

Materials and Methods

S1. Current water reservoirs and D/H compositions

The size of the current exchangeable water reservoir is based on the (negligible) concentrations of water vapor in the modern atmosphere; orbital detections of H_2O ice within the volume of the North Polar layered deposits (NPLD) (~12 m GEL; *(6)*), the North Pole Basal Unit (~1.5 m GEL; *(49)*, the South Polar layered deposits (~11 m GEL; *(7)*); and the broader south polar deposits, glaciers, and high- and mid-latitudinal subsurface ice *(50)*. Most estimate that mid-latitudinal ice deposits contain <1-1.1 m GEL *(51-54)*. Thus, the minimum size of the current water reservoir is the volume of NPLD and SPLD (~20 m GEL). However, it has also been suggested that the total south polar water reservoir may be twice as large as the total north polar reservoir and that mid-latitudinal glaciers and subsurface ice may be larger reservoirs, collectively totaling ~35 m GEL *(8)*. As the size of the modern surface exchangeable reservoir is a subject of study, we conservatively allow a maximum size of 40 m GEL.

The present-day D/H composition has been evaluated by astronomical global and latitudinal measurements *(9,11,55)*, atmospheric and surface fine samples measured with the Sample Analysis at Mars (SAM) instrument on the Curiosity rover *(10,56)*, and measurements of young Shergottite, Nakhlite, and Chassignite (SNC) meteorites *(19,57)* (Fig. S1). Global averages from telescopic data combined with models are estimated to be 6 ± 3 × SMOW *(55)* or 5.2 ± 0.2 × SMOW *(9)*. Latitudinal seasonal differences in atmospheric D/H of 1-10 × SMOW have been observed, with a general global value of 7 × SMOW *(11)*. Most of the exchangeable reservoir is present in the NPLD and SPLD today. The NPLD has been modelled to have D/H compositions of 2.7 – 8 × SMOW *(11,58-59)*. SAM measurements of the atmosphere yielded 5.95 ± 1 × SMOW *(10)* while measurements of surface fines yielded 4.8-8 × SMOW *(10,56)*. Young meteorites with ages <1 Ga record a range of 5-7 × SMOW *(19,57)*. Hence, estimated D/H compositions of the exchangeable reservoir today vary considerably based on observational methods. We approximate the present-day D/H composition of the exchangeable reservoir with the estimates that range from 5-10 × SMOW (Fig. S1) *(9-11,19,55-59)*.

S2. Initial and Hesperian atmospheric D/H composition

D/H measurements within the ALH84001 meteorite (3.9-4.1 Ga; *(61-62)*) provide the oldest available measurement of D/H of the Martian atmosphere, yielding D/H compositions of 4 × SMOW or 2 × SMOW based on Secondary Ion Mass Spectrometry (SIMS) analysis of apatites and carbonates, respectively (Fig. S1, Table S1) *(12-13)*. The only other meteorite, NWA7034 (Black Beauty), which contains materials of similar age (~4.4 Ga) does not record atmospheric D/H values *(63-64)*.

SAM has measured several rock samples for hydrogen isotopes using its Tunable Laser Spectrometer (TLS) and Quadruple Mass Spectrometer (QMS). TLS measurement of the Cumberland sample has been used to infer a D/H composition of 3 ± 0.2 × SMOW *(60)* for the exchangeable reservoir during sediment deposition in Gale Crater (3.5-2.6 Ga *(65-67))*. This measurement was part of a combustion experiment in which only water released at 550°C and 920°C was analyzed *(60)*. Water released in this temperature range is inferred to be the structural hydroxyl hydrogen from the octrahedral layer of smectite *(60)*. In general, SAM measurements will only record the D/H composition of the ancient surface environment in combustion experiments performed at high temperature, as water released at lower combustion temperatures would be from a range of mineral sources and yield high, modern atmospheric D/H values *(60)*.

Samples from rock strata explored later in the mission were also measured with the TLS at high combustion temperatures of 374-862°C associated with dehydroxylation of clay minerals and include Cumberland, Quela, Duluth, Kilmarie, and Glen Etive samples. These yield a D/H range of 3-5 × SMOW (Fig. S1) available on the Planetary Data System (PDS) as SAM TLS level 2 data, following processing and corrections according to *(60,68).* We adopt 3-5 × SMOW as the D/H range for mineralization within lake sediments in Gale Crater.

We adopt the age of ALH84001 (~4.1 Ga) as our model starting point as this is the earliest data point for the atmosphere, corresponds approximately to the earliest geologic units *(69),* and occurs after the generally unconstrained conditions of the Pre-Noachian. We do not enforce any constraints on the composition of the exchangeable reservoir during the Hesperian, unlike previous studies *(15,40).* This is due to the large uncertainty in the SAM data that still needs to undergo a detailed assignment of mineral sources for released water. However, we do perform a qualitative comparison between model simulations and the 3-5 × SMOW range of all SAM data measured from high temperature combustion experiments (Fig. 2, Fig. 3).

S3. Crustal hydration volume

Remote sensing data show globally widespread hydration of the upper crust of Mars during the Noachian, exhibited by hydrated minerals exposed from current crustal depths of 7-10 km in the walls of tectonic features like Valles Marineris and central uplifts of complex craters and basins *(18,70-71)*. More geographically restricted hydrated mineral formation continued during the Hesperian, observed at the Meridiani and Gale crater landing sites as well as in Hesperian and early Amazonian hydrated mineral deposits seen from orbit *(18,44,65-67,72).* Observations at the Gale landing site support water contents of 1-5 wt. % in stratigraphic units *(72-74),* and infrared and neutron spectrometer data acquired globally show water contents of 2.5-9 wt.% and 2-15 wt. % in the upper half-meter of ice-free terrains, respectively *(75-76)*. Meteorite NWA7034, an aqueously altered crustal regolith breccia, contains ~0.6 wt% bulk water content *(77-78).* More conservative estimates report an average crustal water content range of 0.5-3 wt% *(18,79),* which we adopt as bounding scenarios of hydrated mineral formation to depths of 5-10 km during the Noachian, yielding a range of 100-900 m GEL, i.e., loss of 0.25-2.25 m GEL Myr^{-1} to Noachian crustal hydration (Fig. 1, Table S1). Similarly, this range of water contents for a scenario of hydrated mineral formation to depths of 1 km during the Hesperian yields a range of 10-100 m GEL of water or a loss of 0.014 – 0.14 m GEL Myr^{-1} to Hesperian crustal hydration (Table S1) *(18)*. Amazonian crustal hydration also likely occurred but, due to limited water and limited erosion rates, was restricted to the uppermost crust and was negligible by comparison (a few meters and a few wt. %, totaling $\lesssim$1 m GEL).

The observational range of crustal hydration volumes is consistent with the 400 m GEL water reservoir proposed to have been incorporated within the crust to form serpentines *(80)*. Later observations have shown smectite clays and hydrous phases other than serpentine are more volumetrically dominant (see section S4).

It is possible that crustal hydration could initially have occurred as unexchangeable subsurface ice or water volumes trapped in the subsurface and out of contact with the active hydrosphere *(40,81-82).* Some models have hypothesized an undetected subsurface water/ice reservoir of 100-1000 m GEL *(4,81-82),* and 100s of m GEL subsurface water might be present on Mars today *(81-82)*. While such large quantities of subsurface ice or water have not been directly observed, these estimated volumes are within the range of the observed amount of hydrated minerals within the Martian crust. One possibility is that the majority of subsurface

water/ice could eventually have been incorporated into the crust in the form of hydrated minerals. As such, the crustal hydration reservoir presented in our model (Fig. 1) reflects the entire reservoir of unexchangeable water, approximated as a single reservoir. Observations indicate some or all of this water is as mineral structural water but any as-yet-unobserved deep subsurface ice or deep liquid water would also be part of this reservoir.

S4. D/H fractionation associated with crustal hydration

Fe/Mg-smectite clays are the most volumetrically abundant hydrated minerals on Mars by orders of magnitude *(44-45,72-74,83)*, and their formation would cause a D/H fractionation of the exchangeable reservoir. Clays preferentially incorporate hydrogen into their crystal structure over deuterium, which is approximated by the equilibrium fractionation factor between water and smectite ($\propto_{smectite-H_2O}$). Geochemical experiments and models that evaluate this fractionation factor span a possible range of 0.91-0.99 for $\propto_{smectite-H_2O}$ (Table S3). These fractionation factors have generally been evaluated for Al-rich smectites, commonly formed on Earth, as opposed to Fe/Mg-rich smectites, commonly formed on Mars. Fe-rich smectites yield fractionation factors of 0.91, while Al-rich smectites yield higher fractionation factors of 0.98 *(86)*. No experimental constraints are available on the fractionation factors related to the exact chemical composition of smectites on Mars. However given the restricted possible range of fractionation factors (0.91-0.99), we adopt the median value of $\propto_{smectite-H_2O} = 0.95$ as our assumed approximation of the exchange between the exchangeable reservoir and Fe/Mg-smectites on Mars (Table S1).

S5. Volcanic degassing volume

The volcanic degassing through geological time has previously been estimated by photogeology and by modelling the thermophysical and chemical evolution of the mantle and crust. The initial upper mantle temperature governed the amount and timing of water loss from the mantle *(90)*. two models have been proposed *(24)* that differ in assumptions regarding the surface fraction (f_p) of "hot upwellings" in which melting is taking place, which changes the time-dependence of volcanism and cumulative volatile release. Assuming an initial mantle water content (f_{mantle}) of 100 ppm, melting on a global scale (f_p = 1; "the Global Melts model") results in 61 GEL of degassed water while melting restricted to mantle plumes (f_p = 0.01; "the Mantle Plume model") results in 17 GEL of degassed water *(24)* (Fig. 3). Time-dependent degassing curves estimated by *(90)* with 15-25 GEL outgassing are similar to the Mantle Plume model, when assuming an initial mantle water content of 100 ppm, and are encompassed by this scenario. These models also match within uncertainties the photogeological estimates of crustal production rates *(91-92)*.

Volcanic degassing models scale directly with assumed initial water content (f_{mantle}) of the volcanic source region, which is constrained by Martian meteorite data. These data reveal a possible range of water contents in source regions from few ppm to 1000 ppm *(36)* (Table S1). Previous works adopted 100 ppm *(24,93)*. However, assuming mantle water contents of 1000 ppm, which are extreme but within proposed ranges *(36,94)*, the Mantle Plume model and Global Melts model would yield 170 and 610 GEL outgassed water, respectively. For the difference in time-dependent degassing, we utilize the Global Melts model scaled to 300 ppm instead as an upper bound – equivalent in cumulative degassing to the Mantle Plume model at 1000 ppm (Fig. 3).

With these 4 different volcanic degassing models (Fig. 3), we provide representative time-dependent volcanic outgassing fluxes ($F_{volcanic}$) scenarios that bracket all previously proposed

models (Table S1) *(24,90-93,95)*. Volcanic outgassing of H_2O is also dependent on redox conditions *(96-97)* as well as mantle overturn and heterogeneity *(98)* adding additional uncertainty. In general, these one-dimensional volcanic degassing models (Fig. 3) are first-order approximations. The effects of other relevant magmatic model parameters (e.g., outgassing efficiency, initial temperature profiles, thermal properties of the mantle, and crustal thickness, and 3D processes) are encompassed by the parameters that we vary: melt fraction, water content, and timing (Fig. 3, Table S1). These scenarios are representative of the general range of model results that suggest either 40-80 % *(93,95)* or 5-10% *(90)* of the initial mantle reservoir has outgassed through time.

From 0-2.5 Ga, the volcanic degassing in our simulations is changed from the thermochemical model *(24)* because these predict no crustal production during this time interval. To account for observations of Middle-Late Amazonian-formed volcanic units on the surface, during the Amazonian time interval, we instead utilize a surface melt production 0.1 km^3 $year^{-1}$ *(91,99)* and f_{mantle} of 100 ppm yielding an Amazonian volcanic degassing flux $F_{volcanic,A}$ of 2×10^{-4} m GEL Myr^{-1} (Table S1). In comparison, the assumed Amazonian escape flux of 5×10^{26} H atoms s^{-1} is equivalent to the loss of 1.6×10^{-3} m GEL Myr^{-1}; the loss rate greater than degassing rate results in slight increases to the D/H composition of the exchangeable reservoir during the Amazonian (Fig. 2 and Fig. 3).

S6. D/H composition of volcanic gas

We assume that the D/H composition of the Martian mantle dictates the D/H of outgassed waters and is constrained by measuring the D/H composition of water-containing phases, e.g., melt inclusions, glasses, apatites, amphiboles, and biotites, in Martian meteorites. Previous studies have used the lowest measured D/H composition to represent the mantle/igneous end-member of a D/H mixing line, recording exchange between multiple D/H reservoirs *(19,47,64)*. These analyses provide an upper bound on the D/H composition of the mantle (R_{mantle}), yielding a large range of possible D/H values from ~0.8-2 × SMOW for the mantle (Fig. S1, Table S1) *(100)*, which we include as lower and upper bounds in our model. We adopt the result of D/H = 1.275 × SMOW from melt inclusions within shergottites *(47)* as a representative value for the mantle and a middle-case scenario in our preferred model.

We do not model fractionation of D/H compositions in outgassed water compared to the initial source nor any fractionation dependency on the redox state of the melt. Fractionation between water vapor and water in melts is relatively small (tens of permille or maximally up to 100s of permille depending on redox conditions *(23,101-102)*. Compared to the observed isotopic variability within Martian meteorites, these fractionations are negligible for our simulations. Limited retention of water in any crystallizing hydrous mineral phases leads us to assume that most water outgases. This minimizes the effect of any such fractionations if Rayleigh distillation is complete as the accumulated gas will have a D/H composition similar to the initial composition of the melt *(102)*. Assimilation of hydrated minerals or subsurface water within crust that formed prior to the melting event or partial H_2O outgassing within the crust rather than full outgassing of the vapor to the atmosphere may have occurred. This crust could alter the D/H composition of the melt towards the crustal "intermediate" D/H composition (2-3 × SMOW), which has been proposed based on meteorite measurements *(20-21,64)*. However, there is no evidence that pluton formation and melting of pre-existing crust was a widespread phenomenon *(103-104)*. The upper and lower bounds on mantle D/H used in our model

encompass the range that would result with moderate assimilation, partial degassing and redox-dependent fractionation, and the typical mantle D/H.

S7. Present-day atmospheric escape

The present-day H escape flux has previously been measured using instruments aboard the Mars Atmosphere and Volatile EvolutioN (MAVEN) spacecraft (1-11 × 10^{26} H atoms s^{-1}; *(16,105)* and the Ultraviolet and Infrared Atmospheric Spectrometer (SPICAM) aboard the Mars Express spacecraft (10^{25}-10^{27} H atoms s^{-1}; *(17,106-108*). The range of measured H escape fluxes reflects seasonal changes, related to the variable amounts of water vapor at high-altitude on seasonal time scales *(16-17,105-106)*. Dust storms effect this rate, with the escape flux reaching 10^{28} H atoms s^{-1} during the dust storm of MY28 *(105-106)*. The enhanced H escape flux due to dust storms is thought to be related to deep convection and enhanced transport of water vapor to high altitudes *(105-107)*. The integrated present-day H escape fluxes can only account for the loss of few to tens of m GEL water to space *(16-17)*. We adopt the median present-day value of 5 × 10^{26} H atoms s^{-1} for the average H escape flux during the Amazonian ($F_{esc,A}$) (Table S1).

S8. Modelling past Mars H escape fluxes

Most previous studies invoked higher past H escape flux on Mars when considering the high D/H composition of the present-day atmosphere (Fig. S1). However, there have been few attempts to calculate H escape fluxes for Mars during Noachian and Hesperian conditions, presumably due to the large number of unknown parameters. We adapt the input parameters of the pre-existing chemical transport model KINETICS, *(25-26)* for the early Mars atmosphere. The original KINETICS software, including all reactions and rate constants used in this study, is described elsewhere *(25-26)*. We consider the chemistry of 27 species linked by 150 reactions on an altitude grid with 2 km spacing that extends to 240 km. Our model calculates and outputs chemical abundances for each species at every level by computing the chemical production and loss rates at each altitude as well as the diffusive flux between each altitude grid with the 1-D continuity equation:

$$\frac{dn_i}{dt} = P_i - L_i - \frac{\partial \phi_i}{\partial z}, \qquad \text{(S1)}$$

where n_i is the number density of species i, φ_i the vertical flux, P_i the chemical production rate, and L_i the chemical loss rate, all evaluated at time t and altitude z. The vertical flux is given by

$$\phi_i = -D_i\left(\frac{\partial n_i}{\partial z} + \frac{n_i}{H_i} + \frac{1-\alpha_i}{T}\frac{\partial T}{\partial z}n\right) - K\left(\frac{\partial n_i}{\partial z} + \frac{n_i}{H_a} + \frac{1}{T}\frac{\partial T}{\partial z}n\right), \qquad (S2)$$

where D_i is the species' molecular diffusion coefficient, H_i the species' scale height, H_{atm} the atmospheric scale height, α_i the thermal diffusion parameter, K_{zz} the vertical eddy diffusion coefficient, and T the temperature *(109)*. The flux consists of two parts: i) molecular diffusion which can be derived from the molecular theory of ideal gases and ii) eddy transport. We calculate the eddy diffusion coefficient profile using an existing formulation *(110)*. The H escape flux was evaluated using this model with present-day conditions (surface pressure (P_S) of 6.36 mbar, calculated H_2 mixing ratio (M_{H2}) of 3.3 × 10^{-5}, surface temperature (T_{surf}) of 214 K, H_2O concentration profile from derived from calculated saturation vapor pressure), which yielded Φ =

2.9×10^{26} H atoms s^{-1} (1.89×10^{8} $cm^{-2}s^{-1}$), validating the model relative to spacecraft measurements *(16-17)*.

We consider 84 atmospheric environments for ancient Mars by varying the surface pressure as 2, 50, 200, 1000, 2000, 5000 mbar; the surface temperature as 190, 210, 240, 270, 300 K; and the mesospheric temperature as 130, 150, 170 K (Table S2). We consider surface temperatures ≥ 270 K in the 2 mbar case to be unphysical; a sufficiently strong greenhouse effect would not be provided by such a thin atmosphere and the assumption of saturation vapor pressure for water would exceed the total surface pressure. We use a solar spectrum corresponding to 4.4 Ga *(114)*.

For each of the 84 environments, we consider three scenarios. In our standard scenario, we fix the H_2O profile to the saturation vapor pressure and allow the H_2 profile to be computed to steady state.. The standard KINETICS model does not include advection. However, a second scenario injects a high-altitude layer of water vapor (60 ppm centered at 100 km), using published atmospheric profiles *(107)*, and functions as a proxy for advection. This scenario is thought to be caused by dust storms at present-day Mars *(105-108)*, but may be applicable during periods of strong convection in an earlier atmosphere. A third scenario fixes the water vapor profile to the saturation vapor pressure but fixes the surface H_2 mixing ratio to 10^{-3}. This is about two orders of magnitude larger than the present day H_2 mixing ratio *(25)*. However, higher H_2 mixing ratio have been proposed to have been produced via surface processes, such as volcanic outgassing and serpentinization *(e.g. 115)*. For standard and fixed, high surface H_2 scenarios, we calculated steady-state photochemical output, which is typically taken to be from $>10^8$ simulated terrestrial years. We do not consider obliquity cycles, which may affect the steady-state solutions. Because the high-altitude water vapor layer is likely only applicable under transient timescales, we show results after 10^7 seconds (~1 year) as shown in the results of *(107)*.

The dominant source of hydrogen is photolysis of water *(25-26,109)*. In the standard case with water fixed to the saturation vapor pressure, the dominant region for hydrogen production resides near the surface, where water vapor is abundant, but at an altitude sufficiently high that atmospheric extinction of ultraviolet (UV) photons is minimal. In dense atmospheres, escape becomes inefficient as diffusion slows the transport of H_2 to the upper atmosphere. In thin atmospheres, it is easier for hydrogen to diffuse to the exobase, where escape occurs. Hence, under standard conditions, the escape rate is inversely related to the surface pressure (Fig. S3). Atmospheric escape rates increase slightly as the mesospheric temperature is warmed due to the greater thermal energy of H_2 and increased water abundance (Fig. S3). The surface temperature appears less relevant, likely because photolysis is photon-limited at low altitudes and the hydrogen produced is collisionally bound. The mean escape rate appears to decrease at the greatest surface temperatures (Fig. S3), but we attribute this to bias from the six unphysical cases we do not consider. Injecting a high-altitude water layer exposes the water to a greater UV flux, allowing rapid hydrogen production and enhanced escape due to fewer collisions in this less dense region (Fig. S3). Likewise, fixing the surface mixing ratio of H_2 affects the full profile, lofting more to the upper altitudes. The increased presence of high-altitude hydrogen results in an increased escape rate for the denser atmospheres (Fig. S3).

We performed simulations in our D/H model of our entire parameter space, yielding Noachian and Hesperian escape fluxes ranging from 10^{25}-10^{30} H atoms s^{-1}. We find that our D/H model is compatible with a Noachian H escape flux ($F_{esc,N}$) of 10^{25} to 4×10^{29} H atoms s^{-1} and a Hesperian escape flux ($F_{esc,H}$) of 10^{25} to 7×10^{28} H atoms s^{-1} (Table S1, Fig. S3). If past escape fluxes were higher than the ranges presented in Fig. S2, the average of model simulations would produce

much higher present-day D/H values than 10 × SMOW and the full span of model simulation results will vary over 10,000s of ‰, which are not observed for Mars. Lower H escape fluxes than 10^{25} H atoms s^{-1} are improbable, based on higher measured modern escape rates, the KINETICS results, and cannot reproduce modern D/H compositions >5 × SMOW.

S9. D/H fractionation associated with atmospheric escape

H escape causes major fractionation of the atmospheric D/H as hydrogen preferentially escapes compared to deuterium. This fractionation factor, $\propto_{escape}$, can be calculated as

$$\propto_{escape} = \frac{\varphi_D/\varphi_H}{[HDO]_s/2[H_2O]_s} \quad (S3)$$

where, φ_H and φ_D are the escape flux of H and D and $[HDO]_s$and $[H_2O]_s$ are the concentrations of HDO and H_2O at the surface approximating the total amounts of hydrogen and deuterium in the atmosphere *(derivations in 28-30)*. $\propto_{escape}$ describes the relative efficiency of D versus H escape, where H_2 and HD are the dominant escaping species. H_2 primarily sources from H_2O in the Martian atmosphere. Hence, the efficiency of H escape can be written as the H escape flux as a function of the surface concentration of H_2O (and equivalent for the deuterated species). The factor of two in eq S3 derives from a single H_2O molecule sourcing two H atoms, but HDO sourcing only one D atom *(derivations in 28-30)*. These escape fluxes and concentrations have previously been modelled through photochemistry with a range of results: $\propto_{escape}$ = 0.32 *(30)*; 0.016 or 0.135 *(29)*; and ~0.002 *(28)* using revised photochemical models *(107)*. Hence, the range of $\propto_{escape}$ we consider is 0.002-0.32 (Table S1).

S10. Step-wise Rayleigh distillation numerical modelling equations

D/H fractionations related to clay formation and atmospheric escape were evaluated assuming Rayleigh distillation.

$$R = R_0 \times \left(\frac{X}{X_0}\right)^{\propto -1} \quad (S4)$$

where R is the isotope ratio of the residual reservoir, R_0 is the initial isotope ratio, X is the residual amount of the light isotope, X_0 is its initial amount, and α is the fractionation factor. Our model evaluates the isotope ratio at each 10-Myr time step i through eq. S5-S10. First, the size of the exchangeable reservoir X_{ex} at time step i (t_i), where t_0 is the starting point, is evaluated by integrating the time-dependent volcanic degassing rate ($F_{volcanic}$), H escape flux (F_{esc}), and crustal hydration rate (F_{crust}) and accounting for the initial reservoir size ($X_{ex,0}$) (eq S5).

$$X_{ex_i} = X_{ex,0} + \int_{t_0}^{t_i} F_{volcanic,t_i} - \int_{t_0}^{t_i} F_{esc} - \int_{t_0}^{t_i} F_{crust} \quad (S5)$$

Second, the D/H composition of the exchangeable reservoir (R_{ex}) is corrected (R_{mix}) to account for the contribution of depleted volcanic gas (R_{mantle}) by linearly mixing with the composition of the exchangeable reservoir (R_{ex}) in eq S6.

$$R_{mix_i} = \frac{\int_{t_{i-1}}^{t_i} F_{volcanic,t_i}}{X_{ex_i}} \times R_{mantle} + \left(1 - \frac{\int_{t_{i-1}}^{t_i} F_{volcanic,t_i}}{X_{ex_i}}\right) \times R_{ex_i} \quad (S6)$$

Third, fractionation of the exchangeable reservoir related to crustal hydration is then calculated using eq S4 by integrating the rate of crustal hydration (F_{crust}) for the next 10-Myr time step.

$$R_{res_i} = R_{mix_i} \times f_{res_i}^{\propto_{smectite-H_2O}-1} \quad (S7)$$

$$\text{where } f_{res_i} = \left(1 - \frac{\int_{t_i}^{t_{i+1}} F_{crust}}{X_{ex_i}}\right) \quad (S8)$$

We then use mass balance to determine the relationship between the isotopic composition of the exchangeable reservoir and the reservoir of crustal hydration at the time step.

$$R_{mix_i} = R_{crust_i} \times \left(1 - f_{res_i}\right) + R_{res_i} \times f_{res_i} \quad (S9)$$

Rearrangement of eq. S9 provides the isotope composition of the crustal reservoir (R_{crust}) formed at the evaluated time step.

$$R_{crust_i} = \frac{R_{mix_i} - R_{res_i} \times f_{res_i}}{\left(1 - f_{res_i}\right)} \quad (S10)$$

Last, the fractionation related to atmospheric escape is modelled through Rayleigh distillation and calculated by integrating the H escape flux for the current 10-Myr time step.

$$R_{ex_{i+1}} = R_{res_i} \times \left(1 - \frac{\int_{t_i}^{t_{i+1}} F_{esc}}{f_{res_i} \times X_{ex_i}}\right)^{\propto_{escape}-1} \quad (S11)$$

<u>S11 Modelled 3-period time evolution</u>

The model is divided into 3 intervals. Interval 1 (~ 3.7 - 4.1 Ga) simulates the Noachian when the H escape flux ($F_{esc,N}$) was high and the rate of crustal hydration ($F_{crust,N}$) was high (Fig. 1, Table S1). Interval 2 (~ 3.0 - 3.7 Ga) simulates the Hesperian when the H escape flux may have decreased compared to the Noachian ($F_{esc,H}$) and rate of crustal hydration ($F_{crust,H}$) was lower (Fig. 1, Table S1). Interval 3 simulates the Amazonian (now to ~3.0 Ga) where we assume negligible active crustal hydration processes (Fig. 1, Table S1). During the Amazonian interval, we ignore eq. S7-S11 that account for crustal hydration and calculate the D/H composition of the exchangeable reservoir following eq. S12.

$$R_{ex_{i+1}} = R_{mix_i} \times \left(1 - \frac{\int_{t_i}^{t_{i+1}} F_{esc,A}}{X_{ex_i}}\right)^{\propto_{escape}-1} \quad (S12)$$

The absolute age of the Noachian/Hesperian boundary ($t_{N\text{-}H}$) and the Hesperian/Amazonian boundary ($t_{H\text{-}A}$), when crustal hydration ceased, are uncertain. Estimates of $t_{N\text{-}H}$ vary from 3.7 to 3.5 Ga *(116)*; therefore we investigate $t_{N\text{-}H}$ of 3.7 Ga and 3.5 Ga (Fig. 3, Table S1). Estimates of the Hesperian/Amazonian boundary vary from 3.2 to 2 Ga and the Early Amazonian interval

may have occurred between 3.2 and 1 Ga *(116)*. We adapt $t_{H\text{-}A}$ of 3 Ga to represent a short Hesperian interval within the uncertainty *(116)* (Fig. 3, Table S1). We also adapt $t_{H\text{-}A}$ of 1.5 Ga to encompass the crater chronology uncertainties and hydrated mineralogy observed in the early Amazonian *(67)* (Fig. 3, Table S1).

Supplementary Text

S12. Oxygen sinks

Crustal hydration can be an oxygen sink as well as a source of liberated H_2 because both H_2O and OH are incorporated into a mineral structure during hydrated mineral formation. There are a multitude of reactions in which the formation of minerals can liberate H_2 that could have occurred on ancient Mars. The most well-studied of these include serpentinization and the formation of magnetite. Serpentinization reactions alone have a large possible range of ratios of H_2O incorporated into the crust and H_2 released (H_2O_{in}/H_{2out}) that may vary from ~ 4 – 43 *(117)*. During magnetite formation, often coupled to phyllosilicate formation, H_2O_{in}/H_{2out} may be as small as 2 *(43)*. Clay minerals, such as smectites that dominate the Martian crustal reservoir, may also release H_2 due to incorporation of OH-groups. In contrast, minerals such as hydrated sulfates and hydrated silica sequester only H_2O, without releasing any H_2.

We consider this effect on the oxygen and hydrogen balance in our model simulations. In the minimum escape cases (Fig. 4 and Fig. S4-S6) in which the crustal hydration sink dominates over the atmospheric escape sink, the liberation of H_2 would either balance H escape or cause the accumulation of H_2 in the atmosphere. However, any such accumulation of H_2 in the atmosphere would have increased the H escape flux calculated in the KINETICS simulations (Fig. S3), suggesting that the accumulation of H in the atmosphere could be short-lived and readily removed by atmospheric escape. In this scenario many of our simulations do not require an additional oxygen sink in addition to crustal hydration. H_2 present in the atmosphere for a short period after release may provide greenhouse warming *(e.g., 115)*.

In contrast, our simulations, where the atmospheric escape sink dominates over the crustal hydration sink, would likely need additional oxygen sinks (Fig. 4 and Fig. S4-S6). Atmospheric escape of oxygen can account for between 18-58 m GEL of (1 O in each H_2O) *(4,14,16)*. In simulations, where the H escape flux is larger than both the oxygen escape flux by a factor of 2 and the flux of H liberated through crustal hydration, there must be another sink to account for oxygen liberated by water loss. One possibility is the co-occurrence of crustal oxidation with crustal hydration, in particular oxidation of Fe(II) and S_2 in igneous rocks. Oxidation of FeS minerals in the upper crust can account for the oxygen loss of ~10 m GEL of water *(80)*. Oxidation of volcanically degassed H_2S may have consumed oxygen up to 10-15 m GEL of water *(80)*. In addition, *(118)* proposed that oxidation of Fe(II), SO_2, and H_2S within young (<3.5 Ga) sedimentary deposits could account for oxygen loss of 5 m GEL of water.

However, the volumetrically dominant basaltic Martian crust consists of ~20 wt% total iron oxide (FeO_T), including both Fe(II) and Fe(III) components, based on rover and orbital measurements *(119-122)*. Ratios of Fe(III) to total iron (Fe^{3+}/Fe_T) measured in situ are < 0.2-0.3 for basalts with little alternation on Mars and 0.6-0.9 for highly altered basalts *(121)*. Assuming oxidation of 10-60% of all Fe(II) to Fe(III), requiring 0.5 mol O per mol Fe over the entirety of the crustal reservoir (5-10 km global thickness), the upper and lower bounds of the Fe oxidation oxygen sink are 30-380 m GEL. The total oxygen sink could therefore range between 18-470 m GEL; the minimum is set by the minimum amount of escaped oxygen and the maximum is set by

combined maximum oxygen escape and maximum crustal oxidation. In our modeled maximum escape case where the initial reservoir size is 1300 m GEL (Fig. S4-S6), 530 m GEL of H_2O (1 H_2 molecule per H_2O) is lost through atmospheric escape and 740 m GEL of water is lost through crustal hydration. If we assumed an approximate H_2O_{in}/H_{2out} of ~7 *(117)* during crustal hydration, this would cause the liberation of ~100 m GEL of H_2. To balance the integrated H escape sink, a 410 m GEL oxygen sink is then required, within the estimated range for the oxygen sink.

Volcanic degassing could also have been a source of H_2. Simulations at low pressures found that H_2:H_2O ratios of volcanic gas could be approximately between 1:2 and 1:1 for a redox buffer at QFM-2 *(96)*. If conditions were more reduced, the H_2:H_2O ratios of volcanic gas may have been >1. When considering our 4 volcanic degassing models we use (Fig. 3), this could have been an additional integrated H_2 source of approximately 5-120 m GEL with H_2-equivalent water over Martian history. In cases of high volcanic H_2 contribution, as with significant release of crustal H_2 from crustal hydration, the increased atmospheric H_2 levels would cause an increase in the H escape flux. This flux would not require balancing by an oxygen sink, thus lowering the upper bound on the O_2 sink if H_2:H_2O were high in volcanic degassing. However, as the H escape flux increases it would consequently reduce atmospheric H_2 levels, ultimately causing the atmosphere to return to the loss rate before the H_2 outgassing.

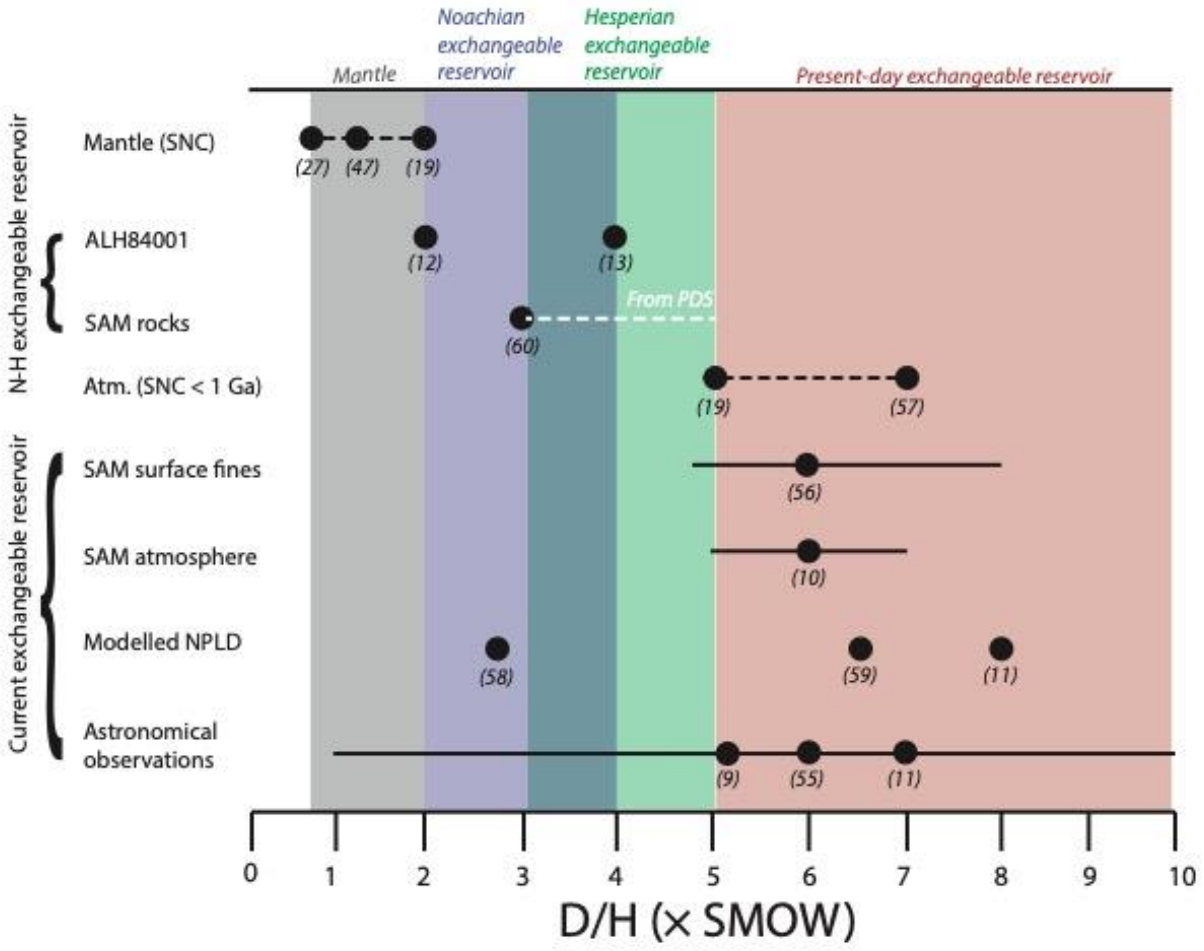

Fig. S1. Previous measurements of Noachian, Hesperian, and current D/H compositions of the exchangeable reservoir. We use these D/H data to provide ranges for the Noachian exchangeable reservoir at 4.1 Ga (blue shading), Hesperian exchangeable reservoir (green shading), the current exchangeable reservoir (red shading), and the mantle (grey shading). Black points show D/H values from previous studies *(9-13,19,27,47,55-60).* Solid black lines for SAM atmosphere shows standard error of mean as given in *(10).* Solid black lines for SAM surface fines shows full data range given in *(56)* while the dot shows the mean of these data. Solid black lines for astronomical observations shows the full range of data given in *(11)*. Dashed black lines indicate multiple measurements within the range of values. Dashed white line shows the range of SAM measurements of high temperature combustion experiments of Hesperian rocks as found on the PDS.

Table S1. Parameter ranges used in simulations of D/H model. This is a summary compilation of all the observational constraints on parameter ranges explored within the D/H model of this study. More details with respect to selected value ranges are given in Materials and Methods sections S1-S11.

Variable	Meaning	Value Range	Units	Reasoning
$R_{ex,0}$	Initial D/H of exchangeable reservoir	2-4 × SMOW	N/A	D/H measurements of ALH84001 *(12-13)*
$R_{ex,end}$	D/H of present-day exchangeable reservoir	5-10 × SMOW	N/A	Compilation of astronomical, meteorite, and SAM data (Fig. S1) *(9-11,55-59)*
R_{mantle}	D/H of mantle	0.8-2 × SMOW	N/A	D/H measurements of various meteorites *(19,27,47,100)*
$\propto_{smectite\text{-}H2O}$	D/H fractionation factor between smectite and water	0.95	N/A	Literary review of geochemical experiments (Table S2) *(84-89)*
$\propto_{escape}$	D/H fractionation factor of atmospheric escape	0.002-0.32	N/A	Compilation of photochemical model results *(28-30)*
$X_{ex,end}$	Present-day size of exchangeable reservoir	20-40	m GEL	Remote sensing evidence *(6-8,49-54)*
$F_{crust,N}$	Rate of water drawdown by crustal hydration during the Noachian	0.25-2.25	m GEL Myr^{-1}	Remote sensing evidence *(18,70-83)*
$F_{crust,H}$	Rate of water drawdown by clay formation during the Hesperian	0.014-0.14	m GEL Myr^{-1}	Remote sensing evidence *(18,70-83)*
f_{mantle}	Water content of mantle	100-1000	ppm	*(24,36,92,94)*
$F_{volcanic}$	Rate of volcanic degassing of H_2O	Time-dependent fluxes, see text	m GEL Myr^{-1}	Compiling thermal evolution models *(24,90-95)*
$F_{volcanic,A}$	Rate of volcanic production after 2.5 Ga	2×10^{-4}	m GEL Myr^{-1}	Remote sensing evidence *(91,99)*
$F_{esc,A}$	Present-day H escape flux	$1\text{-}11\times10^{26}$	H atoms s^{-1}	Measured by MAVEN/Mars Express *(16-17)*
$F_{esc,N}$	H escape flux during the Noachian	$5\times10^{26}\text{-}4\times10^{29}$	H atoms s^{-1}	Modelled in this study (Fig. S2-S3)
$F_{esc,H}$	H escape flux during the Hesperian	$5\times10^{26}\text{-}5\times10^{28}$	H atoms s^{-1}	Modelled in this study (Fig. S2-S3)
$t_{N\text{-}A}$	End of deep, "Noachian" crustal alteration	3.7 - 3.5	Ga	Uncertainty regarding crater statistics *(116)*
$t_{H\text{-}A}$	End of shallow , "Hesperian" crustal alteration	3 - 1.5	Ga	Orbital observations of Hesperian and Amazonian hydrated mineralogy and uncertainty regarding crater statistics *(67,116)*

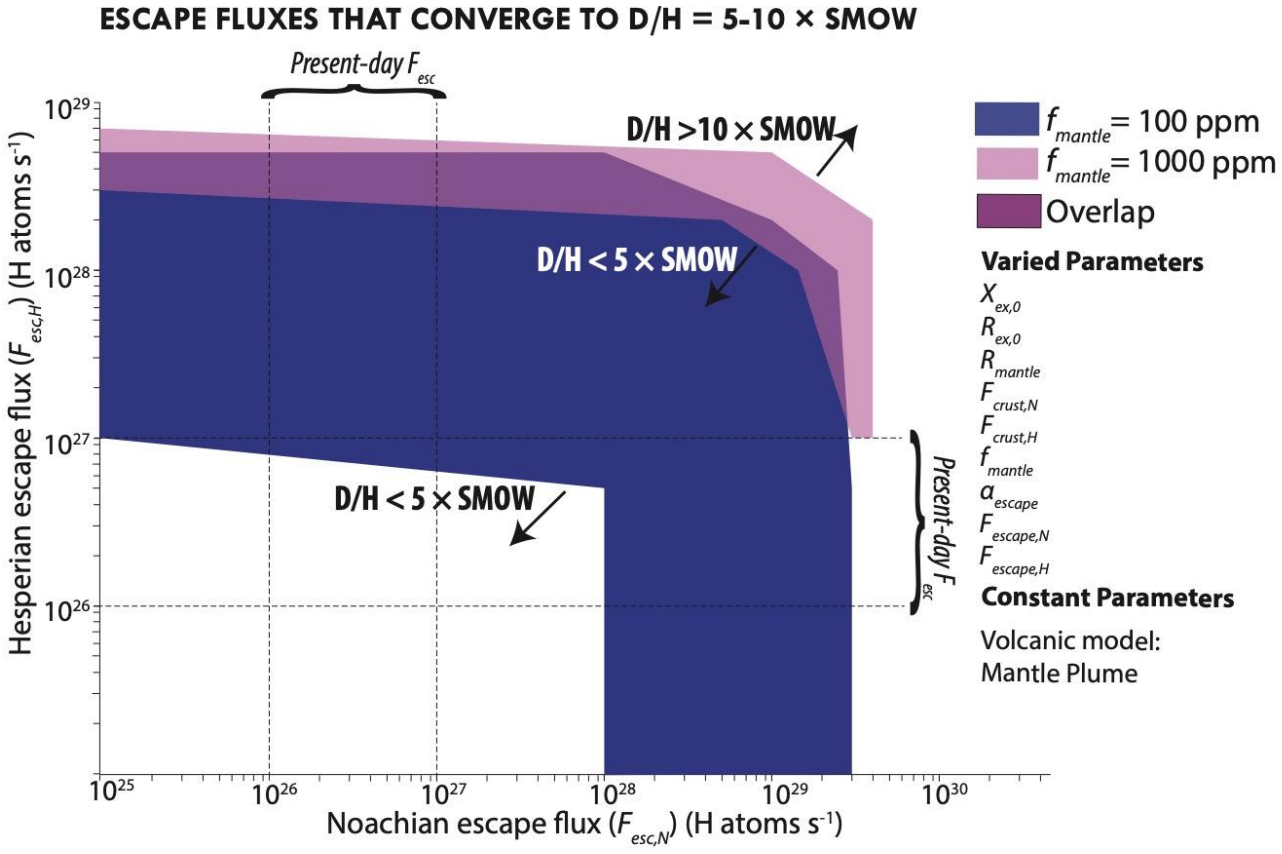

Fig. S2. Hesperian and Noachian escape fluxes in our simulations. Hesperian and Noachian H escape fluxes for the present-day exchangeable reservoir ($R_{ex,end}$) evaluated at the initial D/H compositions ($R_{ex,0}$) between 2 × SMOW and 4 × SMOW and run for the 2 Mantle Plume models. Parameter combinations were accepted when present day D/H was between 5-10 × SMOW, shown where f_{mantle} was assumed 100 ppm (dark blue region) and 1000 ppm (fuchsia region) (Fig. 3) as well as their overlap (purple region). The range of present-day escape fluxes of ~10^{26}-10^{27} H atoms s^{-1} is shown with dashed vertical lines for comparison. Some Noachian and Hesperian escape flux combinations that are similar to present-day escape fluxes satisfy the 5-10 × SMOW convergence condition for the Mantle Plume, f_{mantle} = 100 ppm volcanic degassing model.

Table S2. Parameter ranges used in the KINETICS simulations.

Variable	Meaning	Value	Units	Reasoning
P_s	Surface pressure	0.002 – 5 with intermediate cases of 0.05, 0.2, and 1, 2 bar	Bar	Minimum level based on current pressure *(111)* Intermediate cases consider proposed pressures for early Mars *(22)* Maximum level considers an extreme case
T_s	Surface temperature	190-300	K	Minimum level based on current average temperature *(112)* Maximum level based on room temperature
T_{meso}	Temperature of mesosphere	130-170	K	Extrapolation from temperature structure of atmosphere today *(25,113)*
F_{EUV}	Solar extreme ultraviolet flux	N/A	N/A	Solar spectrum by *(114)*

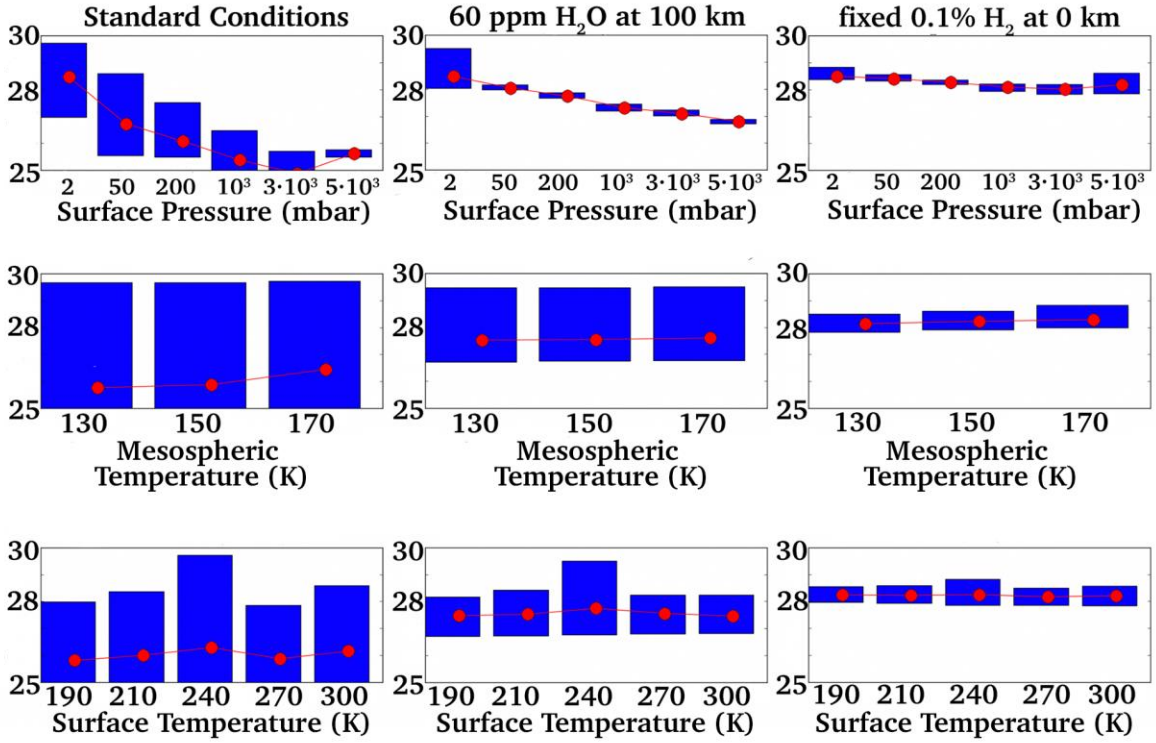

Fig. S3. Results of the KINETICS simulations. Mean global escape rates (red points) in units of H atoms s^{-1}, with the full range (blue bars) spanning from the minimum to maximum escape rates for ranges of surface pressure, mesospheric temperature, surface temperature. Columns show results from the 3 considered scenarios: (A-C) standard ancient Mars (see text), (D-F) high altitude water injection, and (G-I) fixed high surface H_2 mixing ratio of 10^{-3}.

Table S3. Previous experimental measurements of the D/H fractionation between smectite and water ($\propto_{smectite-H_2O}$).

Mineral	Evaluated Expression	$\propto_{smectite-H_2O}$ at 25°C	Reference
Smectite/illite	$1000\ln(\propto) = \frac{-45.3 * 10^3}{T} + 94.7$	0.94	*(84-85)*
Smectite	$1000\ln(\propto) = -65\ to - 10$	0.94-0.99	*(86)*
Al-smectite/Fe-smectite	$1000\ln(\propto) = -20\ to - 90$	0.91-0.98	*(86)*
Smectite/illite	$1000\ln(\propto) = \frac{-19.6 * 10^3}{T} + 25$	0.94	*(87)*
Montmorillonite/kaolinite	$\propto = 0.97$	0.97	*(88)*
Montmorillonite	$\propto = 0.94$	0.94	*(89)*

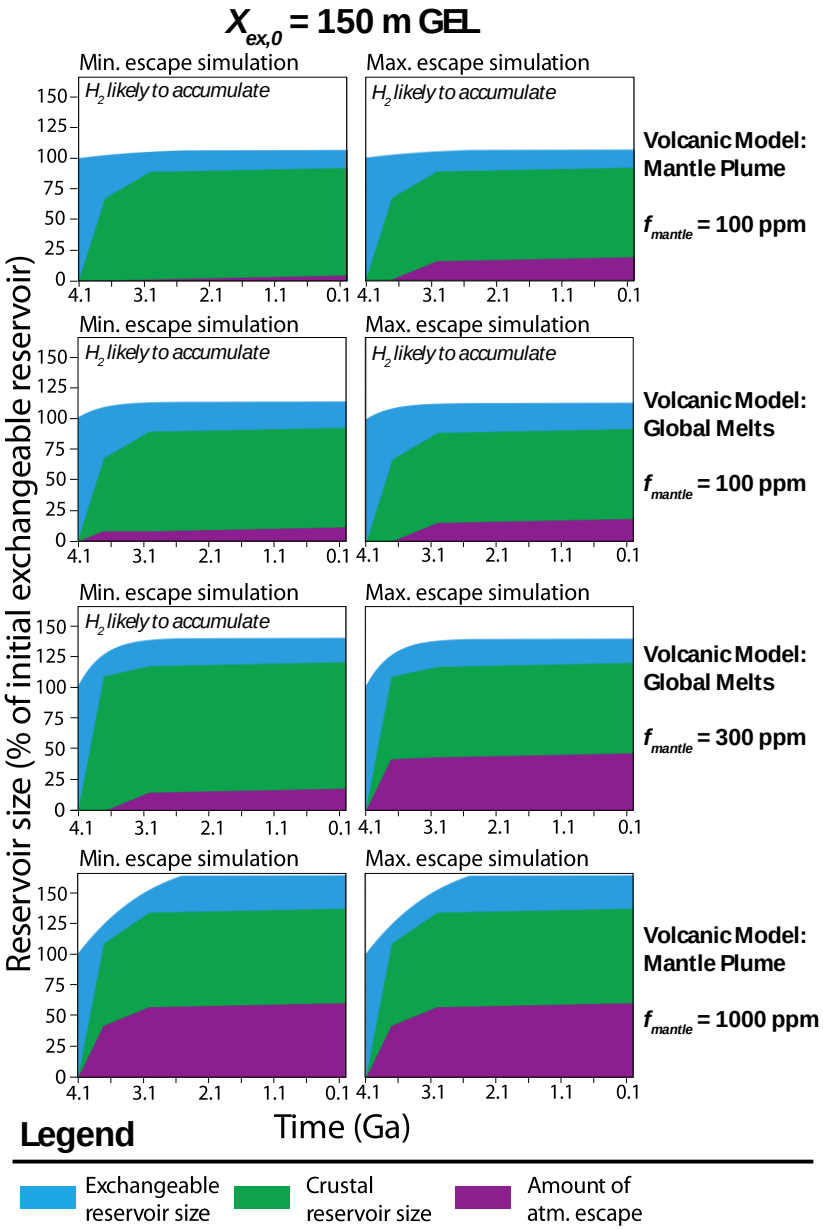

Fig. S4. Cumulative percentage of water in the exchangeable reservoir, crustal reservoir, and escaped water for the full range of model parameters part 1. Same as Fig. 4.C-D but showing results from a different set of parameter combinations. The min. and max. escape simulations from each set of simulations are shown beside each other. Each row of min. and max. escape simulations are organized according to assumptions regarding volcanic degassing model. The initial exchangeable reservoir ($X_{ex,0}$) size was set to be 150 m GEL at 4.1 Ga for all simulations in this figure. All other parameters were varied. In cases where the crustal hydration sink strongly dominates over the atmospheric escape sink, H_2 is likely to accumulate in the exchangeable reservoir. The simulations where H_2 are likely to accumulate have been marked with a sentence inside the figure panel.

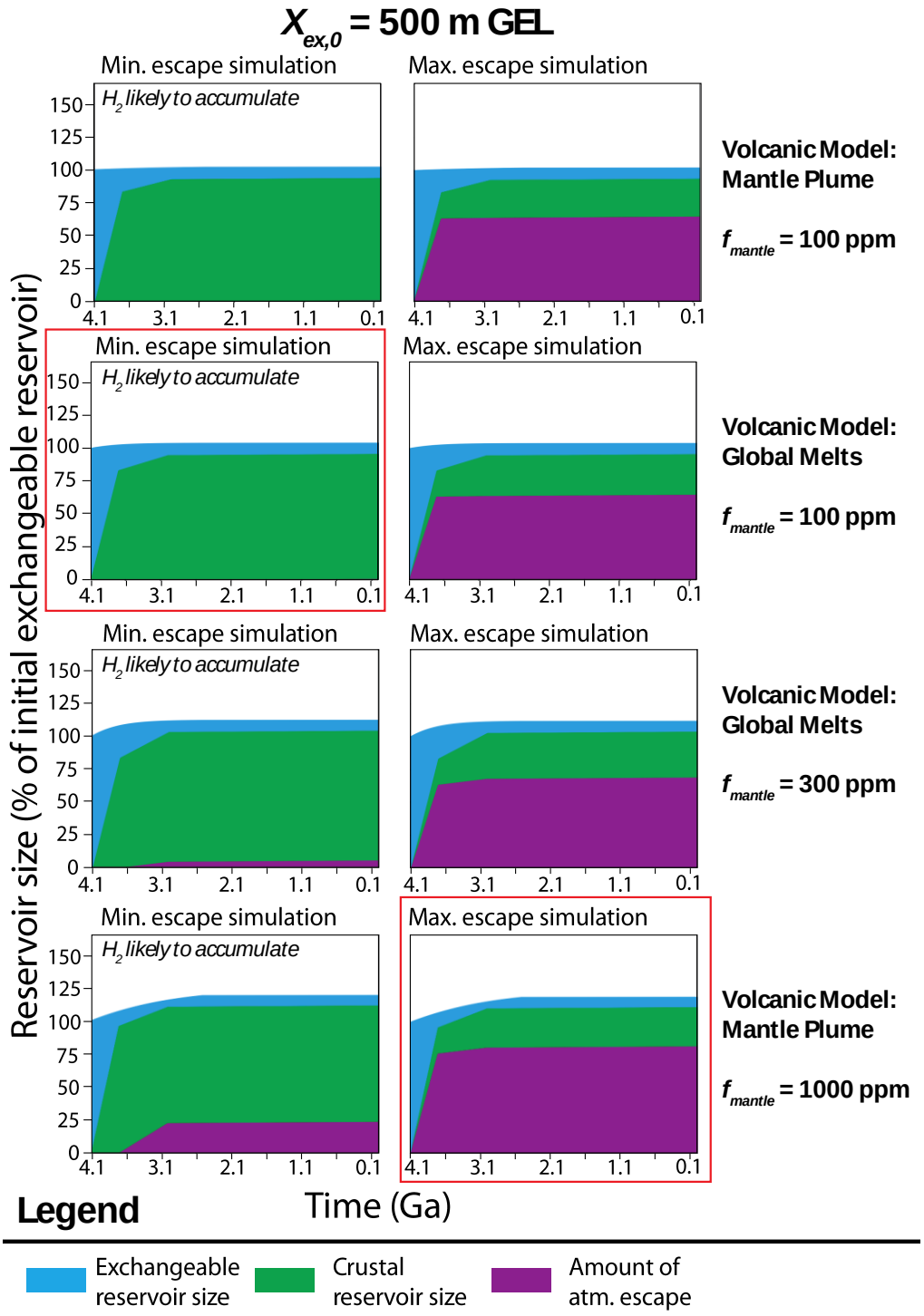

Fig. S5. Cumulative percentage of water in the exchangeable reservoir, crustal reservoir, and escaped water for the full range of model parameters part 2. Same as Fig. S4 but the initial exchangeable reservoir ($X_{ex,0}$) size was set to be 500 m GEL at 4.1 Ga for all simulations in this figure. Plots outlined in red are the minimum and maximum endmembers of the entire examined solution space and are the ones shown in Fig. 4.C-D.

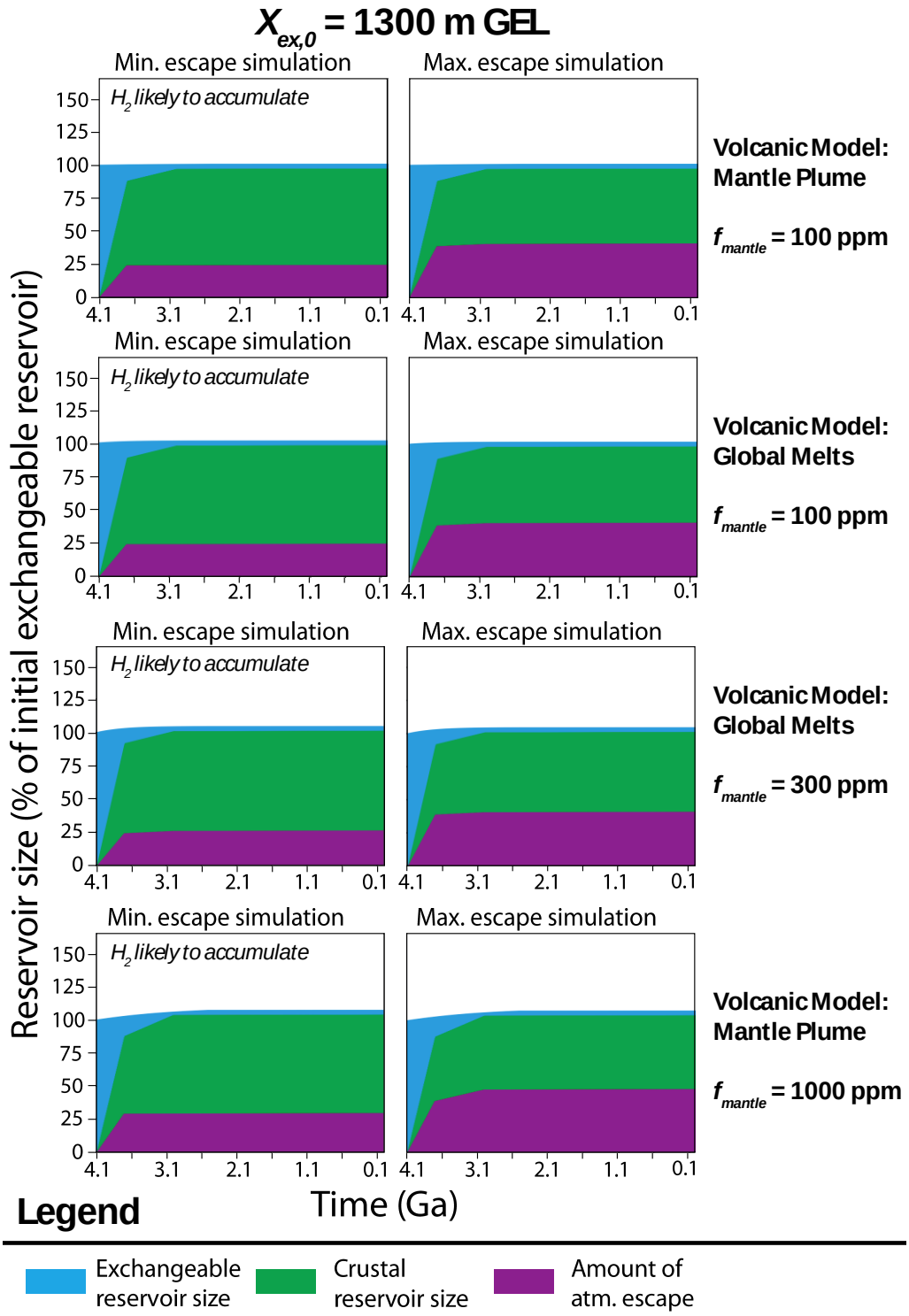

Fig. S6. Cumulative percentage of water in the exchangeable reservoir, crustal reservoir, and escaped water for the full range of model parameters part 3. Same as Fig. S4 but the initial exchangeable reservoir ($X_{ex,0}$) size was set to be 1300 m GEL at 4.1 Ga for all simulations in this figure.